Nano Research

Open Access

Research Article

Carrier funnel switch in quasi-two-dimensional perovskites

Tongqing Sun[1], Junyu He[1], Yang Li[1], Min Li[1], and Xiujuan Zhuang[2]✉

[1] School of Physics and Electronics, Hunan University, Changsha 410082, China
[2] College of Semiconductors (College of Integrated Circuits), Hunan University, Changsha 410082, China

Cite this article: *Nano Research*, **2025**, *18*, 94907070. https://doi.org/10.26599/NR.2025.94907070

ABSTRACT: Quasi-two-dimensional (quasi-2D) perovskites have attracted considerable attention and have been applied to a variety of novel optoelectronic devices due to their specific layered structure and carrier migration properties. Effectively controlling the carrier motion in perovskites with different phases is a crucial factor affecting their optoelectronic performance. Through Cs ions doping, single crystal PEA_2PbI_4 (PEA: phenethylamine) perovskites with n = 1 and n = 2 (n is an integer, representing the number of highly conductive $[PbI]^{4-}$ layers) dule phases have been successfully prepared. It is found that temperature can be used as a switch for the carrier funnel effect of the two phases. At low temperatures, the carrier funnel is open and the carrier is effectively and directionally driven to the n = 2 phase due to the type I bandgap alignment of the heterostructure. As the temperature increases, the bandgap alignment of the heterostructure is carried over to type II, where the carrier channel is closed. Time-resolved photoluminescence (TRPL) spectra show that the highest energy input efficiency is achieved at 80 K. The study provides a feasible strategy for improving the energy transfer efficiency in mixed-phase perovskites.

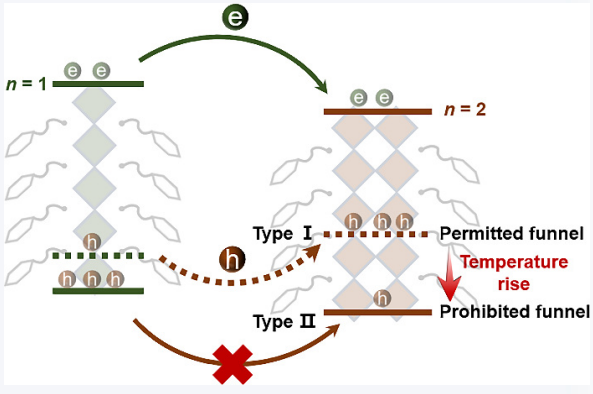

KEYWORDS: quasi-two-dimensional, carrier funnel effect, temperature switch, energy input efficiency

1 Introduction

Organic–inorganic hybrid perovskites is a direct bandgap semiconductor composed of organic and inorganic components self-assembled at a molecular scale. Due to the long carrier diffusion length, high absorption coefficient, high carrier mobility, low trap state, adjustable bandgap and other excellent electrical and optical properties [1–9], organic–inorganic hybrid perovskites have been widely used in the fields of photodetector [10], single photon [11], laser [12]. In particular, the quasi-two-dimensional (quasi-2D) perovskites with chemical formula $L_2A_{n-1}B_nX_{3n+1}$ [13–15] have become a research hotspot owing to their good environmental stability, quantum confinement effect and flexibility [16–21]. Where L is a large aliphatic or aromatic alkyl ammonium cation, such as phenethylamine (PEA), as an insulating medium; A is a smaller monovalent cation, such as cesium (Cs) and methylammonium (MA); B is a divalent metal cation, such as lead (Pb) or tin (Sn); X is the halide anion (Cl, Br, or I); n is an integer, representing the number of highly conductive $[BX_6]^{4-}$ layers [22–24]. Quasi-2D perovskites have a natural quantum well structure and the quantum confinement degree can be tuned by changing the n value so that excitons' absorption/emission energy can be continuously adjusted [24, 25]. Pure phase quasi-2D perovskites are challenging to form and generally consist of mixed phases with different n values. These species with different n values form heterostructure regions and exhibit different band structure alignments, making these heterostructures suitable for different functional devices [26]. For example, the type I structure is more suitable for carrier aggregation and is used to make light-emitting devices [27]. The type II structure is more conducive to carrier migration, resulting in a certain degree of fluorescence quenching, which is more suitable for producing fast-response electronic devices [28]. However, for the heterostructure composed of two perovskite materials, n = 1 and n = 2, there has been controversy over type I and type II structures [29–33]. The carrier transfer efficiency depends on the alignment of the bandgap and the factors that affect the size and relative position of the bandgap will change the carrier transfer channel and affect the luminescence efficiency [25, 34]. It is vital to understand and control the carrier transfer efficiency in quasi-2D perovskites with different n values [35].

Here, the single crystal 2D PEA_2PbI_4 perovskites were prepared by an antisolvent-assisted crystallization approach. Mixed phase

Received: August 11, 2024; **Revised:** September 20, 2024
Accepted: October 11, 2024

✉Address correspondence to zhuangxj@hnu.edu.cn

quasi-2D perovskites with different n values were prepared by doping Cs ions. Excitation power density-dependent photoluminescence (PL), temperature-dependent PL and time-resolved PL (TRPL) experiments were used to analyze and discuss the evolution of the exciton spectrum and carrier transfer in heterostructures. We observe strong temperature dependence and bandgap behavior of emission peaks with different n values by temperature-dependent PL spectra. The energy transfer process between the two phases was studied using TRPL spectroscopy. We find that the heterostructure arrangement is not just type I or type II but changes from type I to type II with increased temperature, which hinders the carrier transfer channel. Therefore, the temperature can adjust the alignment of heterostructures to control the carrier funnel opening and closing. The results provide new insights into the carrier funnel effect of mixed-phase perovskites heterostructures, propose an effective strategy for improving the emission performance of quasi-2D perovskites and have important significance for the development of low-temperature optoelectronic devices based on quasi-2D perovskites.

2 Experimental

2.1 Material preparation

PEA_2PbI_4 and Cs:PEA_2PbI_4 perovskites single crystals were synthesized by antisolvent-assisted crystallization. All chemicals and reagents were purchased from Sigma-Aldrich. Taking PEA_2PbI_4 as an example, PEAI and PbI_2 were dissolved in 5 mL acetonitrile at the molar ratio of 2:1 and the precursor solution was obtained by continuous stirring for 12 h. 0.5 mL of the precursor solution was dropped into the transparent reagent bottle and toluene was added to the solution to begin to precipitate. The supernatant drops were taken on the glass sheet and the glass sheet was put on the heating table at 50 °C to dry. With the evaporation of the solvent, large-size PEA_2PbI_4 perovskites single crystals grew on the substrate. A similar method was adopted to synthesize Cs:PEA_2PbI_4 perovskites single crystal and the initial precursor solution was obtained by adding CsI proportional to PEAI into the precursor solution.

2.2 Micro area PL and TRPL spectra

Steady-state PL spectra were measured using a confocal microscope (WITec, alpha-300) and the fundamental excitation source was a mode-locked Ti: sapphire laser (Tsunami 3941-X1BB, Spectra-Physics) (pulse width 100 fs, repetition rate 80 MHz). The 400 nm excitation light was generated by the second harmonic of an 800 nm laser from a mode-locked oscillator (Tsunami 3941-X1BB, Spectra-Physics) after a bairum boron oxide (BBO) crystal. Then, the laser beam was introduced to a confocal microscope (WITec, alpha-300) equipped with a cryostat (ST-500, Janis Research Company) and focused onto the samples with an objective lens (50 ×, Zeiss, 0.75 NA). The PL emission was collected using the same objective lens. The PL spectra were collected by a spectrometer with 150 g·mm^{-1} grating. The TRPL spectroscopy of the sample was measured using the same optical microscope (WITec, alpha-300) equipped with a streak camera (C10910, Hamamatsu). The fluorescence signal of the sample located in the cryostat (ST-500, Janis Research Company) was guided into the streak camera for time-resolved spectral measurement. The excitation power density measured by all TRPL was ~ 1.88 W·cm^{-2}.

3 Results and discussion

Single crystal PEA_2PbI_4 perovskites with n = 1 and Cs^+ doped PEA_2PbI_4 (Cs:PEA_2PbI_4) was prepared by an antisolvent-assisted crystallization approach elaborately described in the experimental section (Fig. S1 in the Electronic Supplementary Material (ESM)). This method is usually used for controllable synthesis of high-quality perovskite nanoparticles with regular shapes and smooth surfaces [36–38]. Figure 1(a) shows the structure scheme of a quasi-2D perovskites crystal formed by low-dimensional phase

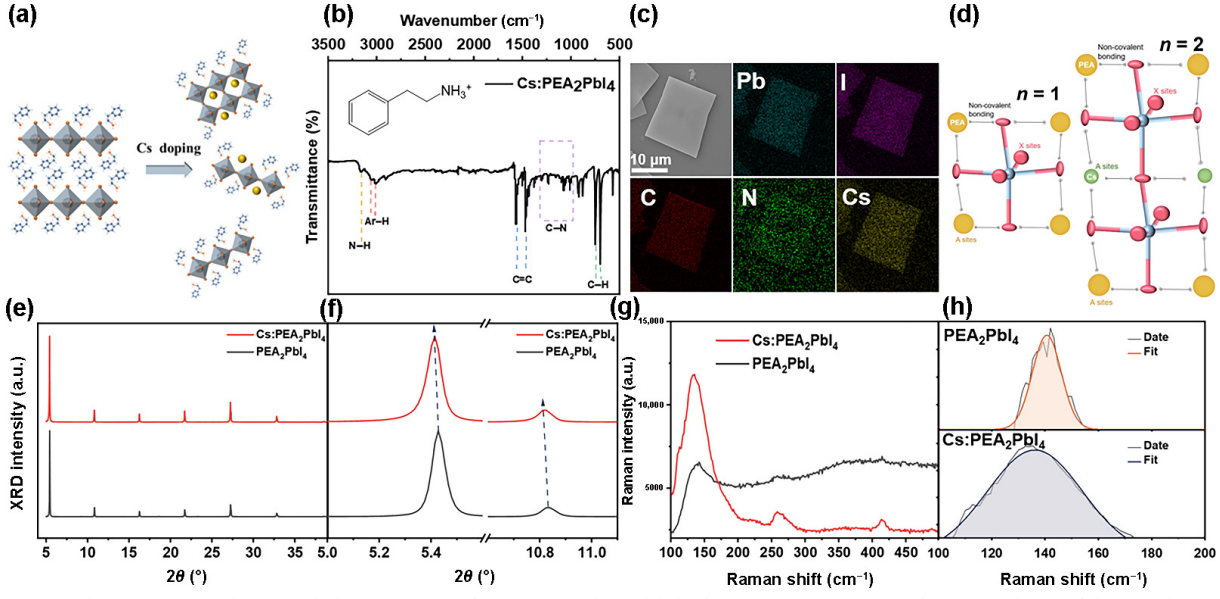

Figure 1 Materials preparation and structural characterization of 2D/quasi-2D layered hybrid organic–inorganic perovskites. (a) Scheme of the crystal structures of perovskites with different n values (n = 1, 2) formed by Cs^+ doping. (b) FTIR transmission spectrum of PEA_2PbI_4. The top left inset shows a schematic structure of PEA^+. (c) SEM image and element mapping of Cs:PEA_2PbI_4. (d) Schematic diagram of expansion of lattice unit by Cs^+ ion doping. (e) XRD patterns of PEA_2PbI_4 and Cs:PEA_2PbI_4. (f) XRD patterns comparison of PEA_2PbI_4 and Cs:PEA_2PbI_4 samples at the diffraction angle 2θ of 5.0°–11.2°. (g) The Raman spectra of PEA_2PbI_4 and Cs:PEA_2PbI_4. (h) Fitting and comparison of 100–200 cm^{-1} Raman shift between PEA_2PbI_4 and Cs:PEA_2PbI_4.

realignment induced by Cs^+ doping. Cs^+ competitively replaces the A-site PEA^+, assembling the previously spaced $[PbI_6]^{4-}$ octahedra to form inorganic layers with $n = 2$ [39]. However, the two phases, $n = 1$ and $n = 2$, cannot be separated entirely and eventually, a heterostructure with mixed two phases co-exists in $Cs:PEA_2PbI_4$ is formed [27, 40].

The morphology and lattice structure of pure PEA_2PbI_4 and $Cs:PEA_2PbI_4$ were systematically characterized by Fourier transform infrared (FTIR) spectrum, scanning electron microscopy (SEM), energy dispersive spectrometer (EDS), element mapping, X-ray diffraction (XRD) and Raman spectra. As confirmed by the FTIR spectra shown in Fig. 1(b), the PEA^+ cation is the dominant organic component of the prepared $Cs:PEA_2PbI_4$ perovskites. The peaks at 1570 and 1470 cm^{-1}, indicated by the blue dashed lines, correspond to the stretching vibration of the C=C bond. The green double peaks at 750 and 698 cm^{-1} are caused by the out-of-plane bending vibrations of the C–H bond on the single substituted benzene ring and the red double peaks at 3060 and 3010 cm^{-1} are caused by the stretching vibrations of the C–H bond in the benzene ring. The purple rectangle and the yellow dashed line are the absorption peaks associated with N, corresponding to the stretching vibration absorption of C–N and the stretching vibration of N–H (3170 cm^{-1}), respectively. To eliminate the influence of the toluene residue of organic solvent, PbI_2 was dissolved in a mixture of acetonitrile and toluene, re-precipitated and its FTIR spectra were determined (Fig. S2 in the ESM). No characteristic peaks representing benzene rings could be found in the obtained spectral peaks, thus proving that all characteristic peaks in Fig. 1(b) were derived from PEA^+ cations in $Cs:PEA_2PbI_4$ rather than toluene residues. Figure S3 in the ESM shows the EDS spectrum of $Cs:PEA_2PbI_4$, which proves that Cs^+ is indeed incorporated into perovskites single crystals and the content is small. The SEM image shows that the $Cs:PEA_2PbI_4$ exhibits a rectangular sheet and the element mapping proves that the elements C, N, I, Pb and Cs are uniformly distributed in the single crystal $Cs:PEA_2PbI_4$ (Fig. 1(c)). Room temperature XRD patterns of 2D and quasi-2D ($n = 2$) perovskites are shown in Fig. 1(e). In PEA_2PbI_4, diffraction angles $2\theta = 5.428, 10.811, 16.313, 21.683, 27.264, 32.805$ are observed and a series of diffraction peaks are obviously related to the (00l) ($l = 2, 4, 6, 8, 10, 12$) plane. These periodic diffusions indicate that the $[PbI_6]^{4-}$ inorganic layer is an equally spaced plane [6, 41]. The XRD pattern of $Cs:PEA_2PbI_4$ also shows an apparent periodicity similar to the diffraction pattern of PEA_2PbI_4. It is worth noting that in the amplified XRD pattern (Fig. 1(f)), the position of the $Cs:PEA_2PbI_4$ diffraction peak moves to a smaller angle. This means that Cs^+ partially replaced PEA^+ at the A-site and the Cs^+ ion as the central atom, which can assemble the $[PbI_6]^{4-}$ octahedron together to form an inorganic layer with $n = 2$ [41, 42], resulting in expansion of the lattice unit, increasing the thickness of the quantum well and increasing the surface spacing, as shown in Fig. 1(d). However, due to the small amount of Cs^+ doping, the lack of diffraction peaks for phases with $n = 2$ does not indicate the absence of these phases, but merely suggests that these phases do not have the long-range crystal periodicity that gives rise to diffract peaks sufficiently strong to be detected by XRD [6]. To further explain Cs^+ in place of PEA^+, Raman spectra of the PEA_2PbI_4 and $Cs:PEA_2PbI_4$ are obtained (Fig. 1(g)). The peaks appearing around 140 cm^{-1} belong to the A_g mode, which is caused by the tensile vibration of the out-of-plane Pb–I bond [43]. The peaks at 260 and 415 cm^{-1} are associated with cationic organic chains [44]. After Cs^+ ion doping, the peak redshifted from 136 to 141 cm^{-1} (Fig. 1(h)), indicating that the $[PbI_6]^{4-}$ octahedron and Cs^+ produced vibrational coupling mode, that is, the bending of inorganic cage caused the vibration of Cs^+ at the A-site [45]. The above results demonstrate that the $Cs:PEA_2PbI_4$ sample is a quasi-2D layered structure with a mixed phase with different n values.

The optical properties of PEA_2PbI_4 and $Cs:PEA_2PbI_4$ were investigated by micro-area PL spectroscopy. Figures 2(a_1) and 2(a_3) show optical photographs of PEA_2PbI_4 and $Cs:PEA_2PbI_4$, respectively. Figures 2(a_2) and 2(a_4) indicate their real-color photographs under 400 nm laser irradiation. Unlike the green light emission in pure PEA_2PbI_4, the $Cs:PEA_2PbI_4$ microplate displays part of the orange light besides the green light emission. The PL spectra in Figs. 2(b) and 2(c) demonstrate that the pure PEA_2PbI_4 exhibits strong single peak emission at a wavelength of 520 nm and the $Cs:PEA_2PbI_4$ has a dual peak emission at 520 and 565 nm, respectively. The PL peak at 520 and 565 nm can correspond to the species $n = 1$ and $n = 2$, respectively, consistent with the previously reported results [6, 46]. The emission peak at 520 nm ($n = 1$) is much more intense than that of 565 nm ($n = 2$), indicating that the carrier radiation recombination mainly occurs in the $n = 1$ layer. Figures 2(b) and 2(c) also display the absorption spectra of the two samples, both of which have obvious features of exciton absorption peaks. In both PEA_2PbI_4 and $Cs:PEA_2PbI_4$, the absorption peak from $n = 1$ appears near 515 nm and the peak from $n = 2$ appears at 560 nm. The 5 nm redshift is caused by the Stokes shift due to phonon scattering. In $Cs:PEA_2PbI_4$, the absorption peak of $n = 1$ is also more significant than that of $n = 2$, indicating that most carriers gather and emission from the $n = 1$ layer. To further elucidate the luminescence mechanism and verify the emerging peak is attributed to the $n = 2$ phase, we have performed excitation power density-dependent PL measurement (Figs. 2(d) and 2(f)). The integral PL intensity of the emission peak as a function of the excitation power density and their linear fitting results are provided in Figs. 2(e) and 2(g). The formula $I_{PL} \sim P^k$ is used to fit the above results, where I_{PL} is PL intensity, P is excitation power density and $k < 1$ for free-to-bound recombination and donor–acceptor pair, $1 < k < 2$ for recombination of excitons (including free excitons and bound excitons) and $k = 2$ for free carrier recombination [47]. The k values are all between 1 and 2, so all emission peaks come from exciton emission [48], indicating that the newly generated peaks and the original peaks of $n = 1$ have the same recombination pathway and it can be further inferred that they come from similar structural phases. The possibility of $CsPbI_3$ luminescence after Cs^+ doping is ruled out because the three-dimensional (3D) perovskite is dominated by free carrier recombination ($k = 2$). At the same time, it is confirmed that these excitation conditions do not involve high-order carrier dynamics, such as biexcitons, Auger recombination or stimulated emission. In summary, the emerging emission peaks can be determined to come from the $n = 2$ phase and all species are excitonic systems. According to the location of the emission peak and previous studies, it can be predicted that phase $n = 1$ and phase $n = 2$ will show a type II band alignment at room temperature [32, 33], as shown in Fig. 2(h). The samples prepared by changing the molar ratio of PEAI, CsI and PbI_2 in the precursor solution have similar PL spectra (Fig. S4 in the ESM) and the position and relative intensity of the emission peaks of $n = 1$ and $n = 2$ phases are basically unchanged.

Temperature-dependent PL spectra of PEA_2PbI_4 and $Cs:PEA_2PbI_4$ were carried out to explore the energy band alignment and the induced carrier transformation process. Excitation power density dependent PL study of PEA_2PbI_4 and $Cs:PEA_2PbI_4$ (Figs. S5

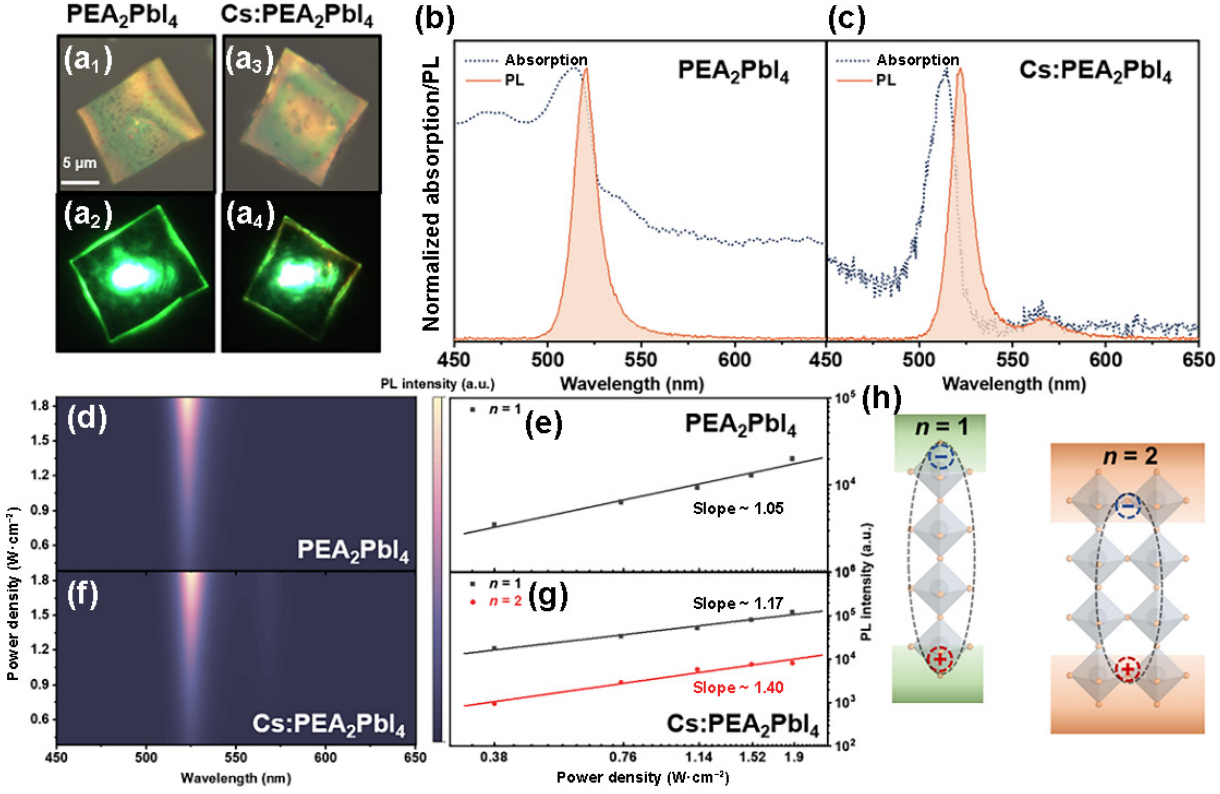

Figure 2 Optical characterization of single crystals PEA_2PbI_4 and Cs:PEA_2PbI_4. (a_1) and (a_3) Optical microscopy images and (a_2) and (a_4) real-color photographs under 400 nm laser excitation. PL spectrum (solid orange lines) and corresponding absorption spectrum (dashed blue lines) of (b) PEA_2PbI_4 and (c) Cs:PEA_2PbI_4. (d) 2D pseudocolor plot of the PEA_2PbI_4 emission spectra under different excitation power density. (e) PL intensity of each peak of PEA_2PbI_4 as a function of excitation power density in a double-logarithmic scale. (f) 2D pseudocolor plot of the Cs:PEA_2PbI_4 emission spectra under different excitation power density. (g) PL intensity of each peak of Cs:PEA_2PbI_4 as a function of excitation power density in a double-logarithmic scale. (h) Scheme of exciton luminescence.

and S6 in the ESM) perovskites single crystals at 80 K show that all samples still maintain exciton system at low temperature. As shown in Figs. 3(a) and 3(c) (top), the PL spectra of PEA_2PbI_4 reach their maximum intensity at 80 K and decrease gradually with an increase in temperature, showing a monotonically decreasing trend. The case for Cs:PEA_2PbI_4 is slightly complicated. As shown in Figs. 3(b) and 3(c) (bottom), the PL peak of $n = 2$ in Cs:PEA_2PbI_4 is similar to that of $n = 1$ in PEA_2PbI_4, that it appears maximum PL intensity at low temperature and monotonically decreases with the increase of temperature. However, its PL intensity of $n = 1$ first increases and reaches a maximum intensity at about 140 K and then decreases when the temperature rises. PL intensity in PEA_2PbI_4 and Cs:PEA_2PbI_4 highly correlates with the exciton density [27, 49]. Usually, the exciton is more stable at low temperatures and exhibits more density, inducing an enhanced PL intensity (Fig. 3(d)). Therefore, it can be inferred from the anomalous intensity change during the heating process of Cs:PEA_2PbI_4 that additional excitons accumulate in the $n = 1$ phase during the initial heating process, significantly enhancing its luminescence intensity.

The temperature-dependent bandgap alignment is further discussed to explore the exciton transfer mechanism in the Cs:PEA_2PbI_4. Figures 4(a) and 4(b) show the pseudocolor graphs of temperature-dependent normalized PL spectra for PEA_2PbI_4 and Cs:PEA_2PbI_4. All the PL peaks for PEA_2PbI_4 and Cs:PEA_2PbI_4 show a blue shift during the temperature rise from 80 to 280 K. The blue shift of the bandgap is due to the lattice expansion effect [50–52]. The thermal expansion of the lattice will weaken the antibond hybridization overlap of the valence band (composed of 6s orbitals of Pb and 5p orbitals of I) with the conduction band (composed of 6p orbitals of Pb and 5p orbitals of I), resulting in the decrease of the valence band bandwidth and the increase of the bandgap [5, 53]. By comparing the PL peak energies at different temperatures, as shown in Figs. 4(c) and 4(d), it can be seen that phase $n = 2$ has a larger offset than phase $n = 1$ of Cs:PEA_2PbI_4. Because $[PbI_6]^{4-}$ in the $n = 1$ phase is sandwiched between two organic layers, it is more constrained (Fig. 4(e)) and the two octahedral cages in phase $n = 2$ are directly connected, making it easier to deform during the thermal expansion (Fig. 4(f)). As a result, the valence band bandwidth in the $n = 2$ phase is significantly reduced and the bandgap blue shift is more extensive, resulting in the bandgap blue shift of phase $n = 1$ and phase $n = 2$ is not synchronized.

In addition to the shift in peak position, the narrowing of PL peaks was observed during cooling. The principal PL peak was fitted with the Gaussian function and the variation of full width at half maximum (FWHM) with temperature is shown in Figs. 4(g) and 4(h). The total PL linewidth is usually described by the sum of the inhomogeneous broadening term Γ_0, the scattering of longitudinal optics (LO) and phonons and the scattering of ionized impurities [44, 53]

$$\Gamma(T) = \Gamma_0 + \gamma_{ac} T + \frac{\gamma_{LO}}{\exp\left(\frac{E_{LO}}{k_B T} - 1\right)} + \gamma_{imp} \exp\left(\frac{-E_{imp}}{k_B T}\right) \quad (1)$$

where Γ is total PL linewidth, T is temperature, k_B is Boltzmann constant. Γ_0 is the line broadening caused by a temperature-independent mechanism, resulting from scattering caused by lattice disorder and imperfections, such as electron–electron interactions,

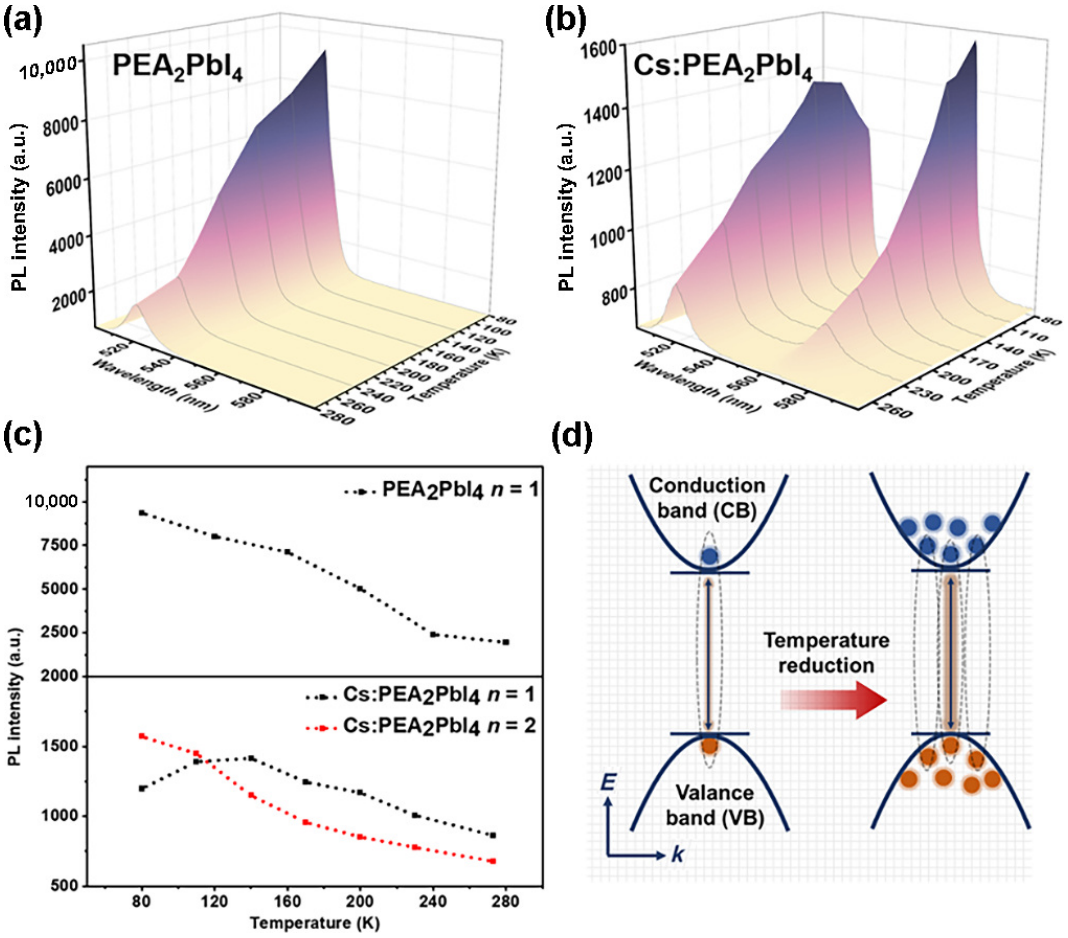

Figure 3 Temperature-dependent PL intensity. 3D mapping of the emission peak intensity for (a) PEA_2PbI_4 and (b) $Cs:PEA_2PbI_4$ at different temperatures. (c) The peak intensity and temperature function are extracted in (a) and (b), in which the top corresponds to PEA_2PbI_4 and the bottom corresponds to $Cs:PEA_2PbI_4$. (d) Scheme of the mechanism of temperature-dependent peak intensity change. *E*: energy. *k*: momentum.

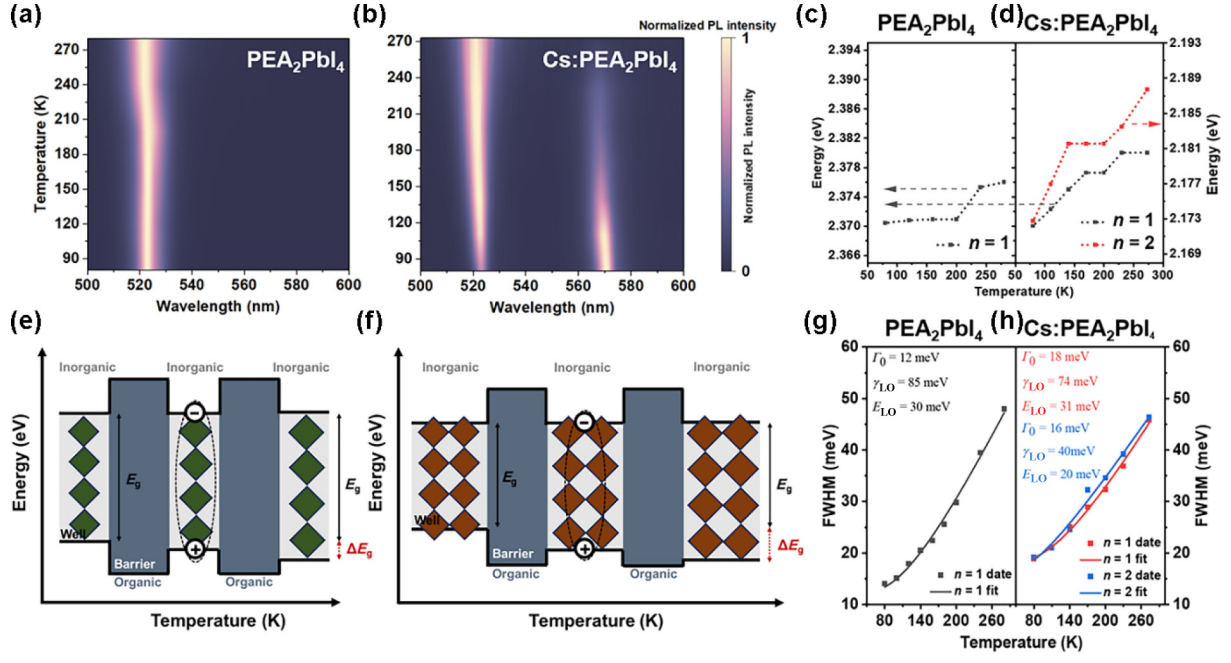

Figure 4 Temperature-dependent bandgap and FWHM. 2D pseudocolor plot of the emission spectra under different temperatures for (a) PEA_2PbI_4 and (b) $Cs:PEA_2PbI_4$. (c) and (d) The function of emission peak energy and temperature extracted in (a) and (b). Scheme of the blueshift of bandgap with temperature in (e) PEA_2PbI_4 and (f) $Cs:PEA_2PbI_4$. E_g: bandgap energy. ΔE_g: bandgap energy difference. The FWHMs of (g) PEA_2PbI_4 and (h) $Cs:PEA_2PbI_4$ extracted from Gaussian fits. The solid line is the fit of the linewidth broadening.

impurities, dislocations, etc. γ_{ac}, γ_{LO} and γ_{imp} are the effective coupling intensity of phonon, photophonon and ionizing impurity scattering, respectively. E_{LO} is the effective optical phonon energy and E_{imp} is the binding energy that binds to ionizing impurity. Each of the terms in Eq. (1) gives a different trend in line widths. Figures 4(e) and 4(f) show that an excellent fit of the temperature-dependent FWHM can be achieved by fully considering the contribution of LO phonons. Therefore, the contribution of phonons and ionizing impurities to FWHM is negligible, consistent with previously reported metal halide perovskites [21, 54–56]. Therefore, Eq. (1) can be simplified as

$$\Gamma(T) = \Gamma_0 + \frac{\gamma_{LO}}{\exp\left(\frac{E_{LO}}{k_B T} - 1\right)} \quad (2)$$

The fitting results are shown in Figs. 4(g) and 4(h) and the fitting results we obtained are similar to those of previous studies [44, 57–59]. Comparing the fitting results of PEA_2PbI_4 and Cs:PEA_2PbI_4, Γ_0 increases slightly in doped samples due to increased impurities. However, the effective phonon energy (~ 30 meV) and phonon coupling strength (~ 80 meV) of the perovskites layer with n = 1 in the two materials are almost the same, indicating that the same phonon is involved in the PL broadening. The electron–phonon interaction can also cause lattice vibration through temperature to change the electron band structure and the electron–phonon interaction will redshift the band gap when the temperature increases. The effective phonon energy (20 meV) and phonon coupling strength (40 meV) of n = 2 is less than that of n = 1. Therefore, the PL redshift caused by electron–phonon coupling and the blueshift caused by thermal expansion are less competitive with each other [21], which makes the blueshift value of the perovskites layer n = 2 larger during the heating process.

TRPL spectroscopy was used to explore the carrier transfer dynamics between n = 1 and n = 2 phases in Cs:PEA_2PbI_4 perovskites. Briefly, single crystal Cs:PEA_2PbI_4 was excited by a femtosecond pulsed laser with a wavelength of 400 nm in a temperature-controlled confocal microscope system and the PL was introduced to a streak camera (see experimental section). The PL dynamic curves of n = 1 and n = 2 at specific temperatures were extracted from the streak camera images, as shown in Figs. 5(a) and 5(b), respectively. Over the measured temperature range, the dynamic curves of the n = 1 phase exhibit PL decay with time constants of a couple hundred picoseconds and PL rise edge with time constants of ~ 10 ps, close to the instrument response function (IRF) (Fig. 5(b)). For the n = 2 phase, the dynamic curves are close to that of n = 1 at room temperature, but it appears to have a significantly prolonged rising edge when the temperature is lower than 170 K (Fig. 5(d)). TRPL characterization of a pure PEA_2PbI_4 sample was compared in Fig. S7 in the ESM, where it shows similar results as the n = 1 phase of Cs:PEA_2PbI_4.

A multi-exponential function with deconvolution of IRF for the dynamic curves fitting and analysis (see Fig. 5(c) and Table S1 in the ESM). For the n = 1 phase of Cs:PEA_2PbI_4, two decay time constants (τ_1 and τ_2), τ_1 ~ 200 ps and τ_2 ~ 400 ps, with positive amplitudes were fitted, corresponding to the carriers' non-radiative and radiative lifetimes, respectively [60, 61]. Both lifetimes first increase and then decrease with the rising temperature because the more active thermal expansion interaction at higher temperatures will prevent exciton recombination and thus increase PL lifetime [5, 53, 62]. As the temperature continues to rise, the decrease in lifetime can be attributed to the exciton–phonon scattering effect [63–65]. For the n = 2 phase, a time constant τ_2 ~ 10 ns with a positive amplitude (A_2) and a time constant τ_0 ~ 250 ps with a negative amplitude (A_{Rise}) were fitted. The significantly prolonged rise time τ_0 implies a carrier transfer process from n = 1 to n = 2 [66–68]. This process corresponds to the PL intensity variation of the n = 1 phase in Cs:PEA_2PbI_4. The carriers' transfer efficiency can be expressed in energy input efficiency (EIE), defined by the carriers' inflow in accepter n = 2 phase as $\eta_{EIE} = \frac{|A_{Rise}|}{A_2 - |A_{Rise}|}$, where η_{EIE} is

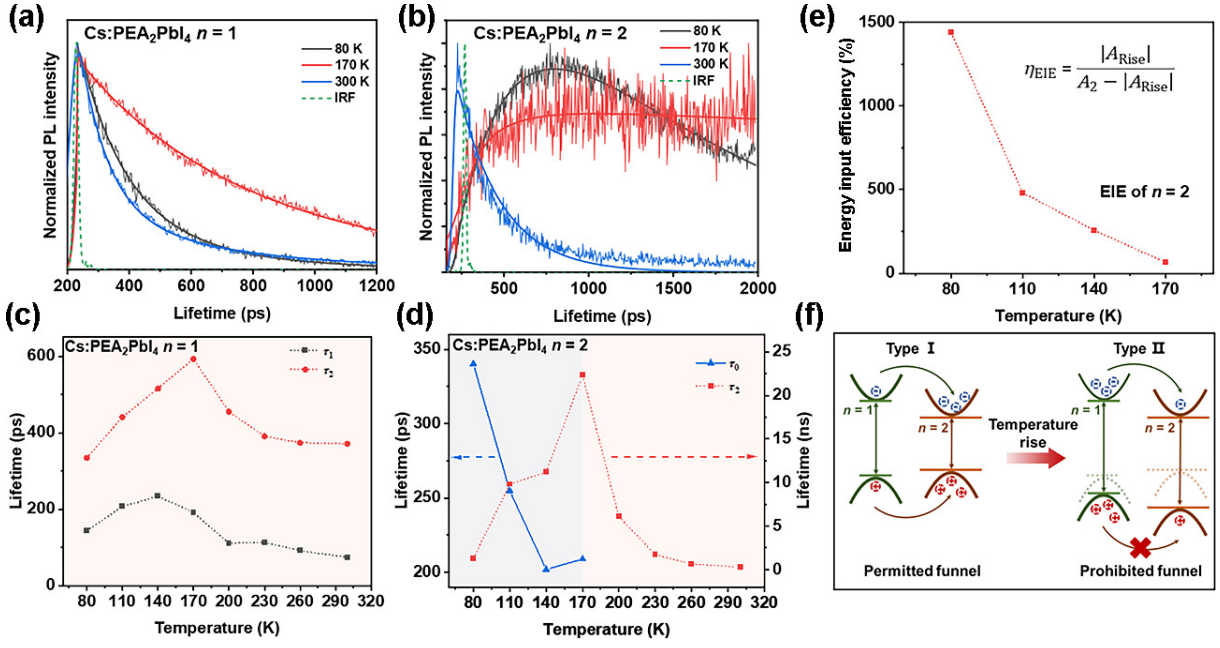

Figure 5 TRPL characterization and the temperature dependence experiments of Cs:PEA_2PbI_4. TRPL curves and their fitting at representative temperatures for (a) n = 1 and (b) n = 2. The fit is using a multi-exponential function (Eq. (1)). Exciton lifetimes of (c) n = 1 and (d) n = 2 as a function of temperature. (e) EIE of n = 2 as a function of the temperature. (f) Schematic illustration of carrier temperature switch.

the population ratio between the energy-transfer-generated carriers and the photo-generated carriers of the $n = 2$ [68]. As shown in Fig. 5(e), the η_{EIE} reaches the highest value at 80 K and decreases gradually with the increase of temperature. Combined with the above analysis, a temperature dependent carriers funnel switch can be schematicly described, as shown in Fig. 5(f). At low temperatures, $n = 1$ phase and $n = 2$ phase are arranged in a type I band structure, which is conducive to the transfer of carriers from $n = 1$ phase to $n = 2$ phase and the PL intensity of $n = 1$ phase is weak. With the increase of temperature, the valence band edge of $n = 2$ phase decreases more than that of $n = 1$ phase and the heterostructures are carried over into type II band alignment, so more excitons are left in $n = 1$ phase for recombination luminescence, resulting in an abnormal increase in the PL spectral intensity of $n = 1$ phase perovskites during the initial heating process. By controlling the temperature, the alignment of the heterostructure can be adjusted to realize the opening and closing of carrier channels so as to improve the energy transfer efficiency.

4 Conclusions

In summary, we have prepared Cs ions doped mixed-phase perovskite structures using a simple antisolvent-assisted crystallization approach and investigated the carrier transfer between $n = 1$ and $n = 2$ phases. Through temperature-dependent spectroscopy, it is found that at low temperatures, the $n = 1$ phase and the $n = 2$ phase are in a type I alignment, which promotes the transfer of carriers to the $n = 2$ phase and weakens the luminescence of the $n = 1$ phase. With the increase in temperature, due to the different sizes of lattice expansion, the blue shift of the two-phase bandgap is not synchronized and the valence band of $n = 2$ phase is gradually lower than that of $n = 1$ phase, forming a type II bandgap alignment and excitons no longer transfer to the low bandgap. TRPL experiments systematically investigated the intrinsic energy transfer of Cs:PEA_2PbI_4 proved that the $n = 2$ phase is indeed filled with carriers after light excitation and gave the energy transfer efficiency of Cs:PEA_2PbI_4. The energy transfer efficiency is the highest at low temperatures and decreases gradually with the increase in temperature. In quasi-2D semiconductors, the carrier funnel is essential in improving device performance. The study provides a new idea for controlling the carrier funnel effect and the carrier separation dynamics can be customized by temperature to achieve controllable emission characteristics.

Electronic Supplementary Material: Supplementary material (details of life fitting; comparison of FTIR transmission spectra of PbI_2 and Cs:PEA_2PbI_4, EDS spectrum of Cs:PEA_2PbI_4, PL spectrum with different precursor ratios, excitation power dependent PL spectra of PEA_2PbI_4 and Cs:PEA_2PbI_4 at 80 K, TRPL characterization and the temperature-dependent experiments of PEA_2PbI_4, fitting results of the dynamic curves) is available in the online version of this article at https://doi.org/10.26599/NR.2025.94907070.

Data availability

All data needed to support the conclusions in the paper are presented in the manuscript and the Electronic Supplementary Material. Additional data related to this paper may be requested from the corresponding author upon request.

Acknowledgements

This work was supported by the National Natural Science Foundation of China (No. 61635001).

Declaration of competing interest

All the contributing authors report no conflict of interests in this work.

Author contribution statement

T. Q. S.: Data curation, validation, writing manuscript, experimental design. J. Y. H.: Data curation, validation. Y. L.: Data curation, project administration. M. L.: validation. X. J. Z.: Project administration, funding acquisition. All the authors have approved the final manuscript.

Use of AI statement

None.

References

[1] Zhou, H. P.; Chen, Q.; Li, G.; Luo, S.; Song, T. B.; Duan, H. S.; Hong, Z. R.; You, J. B.; Liu, Y. S.; Yang, Y. Interface engineering of highly efficient perovskite solar cells. *Science* **2014**, *345*, 542–546.

[2] Stranks, S. D.; Eperon, G. E.; Grancini, G.; Menelaou, C.; Alcocer, M. J. P.; Leijtens, T.; Herz, L. M.; Petrozza, A.; Snaith, H. J. Electron–hole diffusion lengths exceeding 1 micrometer in an organometal trihalide perovskite absorber. *Science* **2013**, *342*, 341–344.

[3] Zhu, H. M.; Fu, Y. P.; Meng, F.; Wu, X. X.; Gong, Z. Z.; Ding, Q.; Gustafsson, M. V.; Trinh, M. T.; Jin, S.; Zhu, X. Y. Lead halide perovskite nanowire lasers with low lasing thresholds and high quality factors. *Nat. Mater.* **2015**, *14*, 636–642.

[4] Xing, G. C.; Mathews, N.; Sun, S. Y.; Lim, S. S.; Lam, Y. M.; Grätzel, M.; Mhaisalkar, S.; Sum, T. C. Long-range balanced electron- and hole-transport lengths in organic–inorganic $CH_3NH_3PbI_3$. *Science* **2013**, *342*, 344–347.

[5] Wehrenfennig, C.; Eperon, G. E.; Johnston, M. B.; Snaith, H. J.; Herz, L. M. High charge carrier mobilities and lifetimes in organolead trihalide perovskites. *Adv. Mater.* **2014**, *26*, 1584–1589.

[6] Fu, Y. P.; Zheng, W. H.; Wang, X. X.; Hautzinger, M. P.; Pan, D. X.; Dang, L. N.; Wright, J. C.; Pan, A. L.; Jin, S. Multicolor heterostructures of two-dimensional layered halide perovskites that show interlayer energy transfer. *J. Am. Chem. Soc.* **2018**, *140*, 15675–15683.

[7] Herz, L. M. Charge-carrier mobilities in metal halide perovskites: Fundamental mechanisms and limits. *ACS Energy Lett.* **2017**, *2*, 1539–1548.

[8] Liu, X. K.; Xu, W. D.; Bai, S.; Jin, Y. Z.; Wang, J. P.; Friend, R. H.; Gao, F. Metal halide perovskites for light-emitting diodes. *Nat. Mater.* **2021**, *20*, 10–21.

[9] Kumar, P.; Thokala, S.; Singh, S. P.; Singh, R. Research progress and challenges in extending the infra-red absorption of perovskite tandem solar cells. *Nano Energy* **2024**, *121*, 109175.

[10] Sun, J.; Ding, L. M. Linearly polarization-sensitive perovskite photodetectors. *Nano-Micro Lett.* **2023**, *15*, 90.

[11] Sakhatskyi, K.; Turedi, B.; Matt, G. J.; Wu, E. F.; Sakhatska, A.; Bartosh, V.; Lintangpradipto, M. N.; Naphade, R.; Shorubalko, I.; Mohammed, O. F. et al. Stable perovskite single-crystal X-ray imaging detectors with single-photon sensitivity. *Nat. Photonics* **2023**, *17*, 510–517.

[12] Zhuge, M. H.; Yin, J.; Liu, Y. L.; Wang, Y. H.; Li, Z. Y.; Xiao, S. M.;

Yu, S. H.; Song, Q. H. Precise control of single-crystal perovskite nanolasers. *Adv. Mater.* **2023**, *35*, 2300344.
[13] Liu, T. F.; Jiang, Y. Y.; Qin, M. C.; Liu, J. X.; Sun, L. L.; Qin, F.; Hu, L.; Xiong, S. X.; Jiang, X. S.; Jiang, F. Y. et al. Tailoring vertical phase distribution of quasi-two-dimensional perovskite films via surface modification of hole-transporting layer. *Nat. Commun.* **2019**, *10*, 878.
[14] Shi, E. Z.; Gao, Y.; Finkenauer, B. P.; Akriti; Coffey, A. H.; Dou, L. T. Two-dimensional halide perovskite nanomaterials and heterostructures. *Chem. Soc. Rev.* **2018**, *47*, 6046–6072.
[15] Li, Z. T.; Cao, K.; Li, J. S.; Tang, Y.; Ding, X. R.; Yu, B. H. Review of blue perovskite light emitting diodes with optimization strategies for perovskite film and device structure. *Opto-Electron. Adv.* **2021**, *4*, 200019.
[16] Lai, H. T.; Kan, B.; Liu, T. T.; Zheng, N.; Xie, Z. Q.; Zhou, T.; Wan, X. J.; Zhang, X. D.; Liu, Y. S.; Chen, Y. S. Two-dimensional ruddlesden-popper perovskite with nanorod-like morphology for solar cells with efficiency exceeding 15%. *J. Am. Chem. Soc.* **2018**, *140*, 11639–11646.
[17] Ren, H.; Yu, S. D.; Chao, L. F.; Xia, Y. D.; Sun, Y. H.; Zuo, S. W.; Li, F.; Niu, T. T.; Yang, Y. G.; Ju, H. X. et al. Efficient and stable ruddlesden-popper perovskite solar cell with tailored interlayer molecular interaction. *Nat. Photonics* **2020**, *14*, 154–163.
[18] Zhou, B.; Yan, D. P. Simultaneous long-persistent blue luminescence and high quantum yield within 2D organic-metal halide perovskite micro/nanosheets. *Angew. Chem., Int. Ed.* **2019**, *58*, 15128–15135.
[19] Li, H.; Lu, J. F.; Zhang, T.; Shen, Y.; Wang, M. K. Cation-assisted restraint of a wide quantum well and interfacial charge accumulation in two-dimensional perovskites. *ACS Energy Lett.* **2018**, *3*, 1815–1823.
[20] Ding, R.; Lyu, Y. X.; Wu, Z. H.; Guo, F.; Io, W. F.; Pang, S. Y.; Zhao, Y. Q.; Mao, J. F.; Wong, M. C.; Hao, J. H. Effective piezo-phototronic enhancement of flexible photodetectors based on 2D hybrid perovskite ferroelectric single-crystalline thin-films. *Adv. Mater.* **2021**, *33*, 2101263.
[21] Tsai, H.; Shrestha, S.; Pan, L.; Huang, H. H.; Strzalka, J.; Williams, D.; Wang, L.; Cao, L. R.; Nie, W. Y. Quasi-2D perovskite crystalline layers for printable direct conversion X-ray imaging. *Adv. Mater.* **2022**, *34*, 2106498.
[22] Chen, Y. N.; Sun, Y.; Peng, J. J.; Tang, J. H.; Zheng, K. B.; Liang, Z. Q. 2D ruddlesden-popper perovskites for optoelectronics. *Adv. Mater.* **2018**, *30*, 1703487.
[23] Guo, R.; Zhu, Z. A.; Boulesbaa, A.; Hao, F.; Puretzky, A.; Xiao, K.; Bao, J. M.; Yao, Y.; Li, W. Z. Synthesis and photoluminescence properties of 2D phenethylammonium lead bromide perovskite nanocrystals. *Small Methods* **2017**, *1*, 1700245.
[24] Park, J. Y.; Song, R. Y.; Liang, J.; Jin, L. R.; Wang, K.; Li, S. R.; Shi, E. Z.; Gao, Y.; Zeller, M.; Teat, S. J. et al. Thickness control of organic semiconductor-incorporated perovskites. *Nat. Chem.* **2023**, *15*, 1745–1753.
[25] Blancon, J. C.; Tsai, H.; Nie, W.; Stoumpos, C. C.; Pedesseau, L.; Katan, C.; Kepenekian, M.; Soe, C. M. M.; Appavoo, K.; Sfeir, M. Y. et al. Extremely efficient internal exciton dissociation through edge states in layered 2D perovskites. *Science* **2017**, *355*, 1288–1292.
[26] Wang, H. Z.; Chen, Y. Y.; Li, D. H. Two/quasi-two-dimensional perovskite-based heterostructures: Construction, properties and applications. *Int. J. Extrem. Manuf.* **2023**, *5*, 012004.
[27] Yuan, M. J.; Quan, L. N.; Comin, R.; Walters, G.; Sabatini, R.; Voznyy, O.; Hoogland, S.; Zhao, Y. B.; Beauregard, E. M.; Kanjanaboos, P. et al. Perovskite energy funnels for efficient light-emitting diodes. *Nat. Nanotechnol.* **2016**, *11*, 872–877.
[28] Lin, R. X.; Wang, Y. R.; Lu, Q. W.; Tang, B. B.; Li, J. Y.; Gao, H.; Gao, Y.; Li, H. J.; Ding, C. Z.; Wen, J. et al. All-perovskite tandem solar cells with 3D/3D bilayer perovskite heterojunction. *Nature* **2023**, *620*, 994–1000.
[29] Posmyk, K.; Zawadzka, N.; Kipczak, Ł.; Dyksik, M.; Surrente, A.; Maude, D. K.; Kazimierczuk, T.; Babiński, A.; Molas, M. R.; Bumrungsan, W. et al. Bright excitonic fine structure in metal-halide perovskites: From two-dimensional to bulk. *J. Am. Chem. Soc.* **2024**, *146*, 4687–4694.
[30] Li, X.; Lin, D. X.; Chen, Z. P.; Li, Z.; Wang, J. M.; Chen, J.; Gong, L.; Xu, J. B.; Chen, K.; Liu, P. Y. et al. Structural regulation for highly efficient and stable perovskite solar cells via mixed-vapor deposition. *ACS Appl. Energy Mater.* **2020**, *3*, 6544–6551.
[31] Quan, L. N.; Zhao, Y. B.; De Arquer, F. P. G.; Sabatini, R.; Walters, G.; Voznyy, O.; Comin, R.; Li, Y. Y.; Fan, J. Z.; Tan, H. R. et al. Tailoring the energy landscape in quasi-2D halide perovskites enables efficient green-light emission. *Nano Lett.* **2017**, *17*, 3701–3709.
[32] Shang, Q. Y.; Wang, Y. N.; Zhong, Y. G.; Mi, Y.; Qin, L.; Zhao, Y. F.; Qiu, X. H.; Liu, X. F.; Zhang, Q. Unveiling structurally engineered carrier dynamics in hybrid quasi-two-dimensional perovskite thin films toward controllable emission. *J. Phys. Chem. Lett.* **2017**, *8*, 4431–4438.
[33] Liu, J. X.; Leng, J.; Wu, K. F.; Zhang, J.; Jin, S. Y. Observation of internal photoinduced electron and hole separation in hybrid two-dimentional perovskite films. *J. Am. Chem. Soc.* **2017**, *139*, 1432–1435.
[34] Ramesh, S.; Giovanni, D.; Righetto, M.; Ye, S. Y.; Fresch, E.; Wang, Y.; Collini, E.; Mathews, N.; Sum, T. C. Tailoring the energy manifold of quasi-two-dimensional perovskites for efficient carrier extraction. *Adv. Energy Mater.* **2022**, *12*, 2103556.
[35] Yao, Y. G.; Zhu, Y. K.; Hu, A.; Gao, Y. N. Temperature-regulated in-plane exciton dynamics in CdSe/CdSeS colloidal quantum well heterostructures. *ACS Photonics* **2023**, *10*, 4052–4060.
[36] Liu, Z. H.; Wang, L.; Xie, X. Y. Improving the performance of inverted two-dimensional perovskite solar cells by adding an anti-solvent into the perovskite precursor. *J. Mater. Chem. C* **2020**, *8*, 11882–11889.
[37] Fu, X. W.; Jiao, S. L.; Jiang, Y.; Li, L. H.; Wang, X. X.; Zhu, C. G.; Ma, C.; Zhao, H. P.; Xu, Z. Y.; Liu, Y. et al. Large-scale growth of ultrathin low-dimensional perovskite nanosheets for high-detectivity photodetectors. *ACS Appl. Mater. Interfaces* **2020**, *12*, 2884–2891.
[38] Yue, Y. F.; Li, M. Y.; Li, H.; Chai, N. Y.; Dong, Y. F.; Li, Z. P.; Chen, X. Y.; Wang, X. W. One-step anti-solvent associated method for high performance two-dimensional perovskite photodetectors fabrication at low temperature. *Chem. Eng. J.* **2022**, *441*, 135997.
[39] Pang, P. Y.; Jin, G. R.; Liang, C.; Wang, B. Z.; Xiang, W.; Zhang, D. L.; Xu, J. W.; Hong, W.; Xiao, Z. W.; Wang, L. et al. Rearranging low-dimensional phase distribution of quasi-2D perovskites for efficient sky-blue perovskite light-emitting diodes. *ACS Nano* **2020**, *14*, 11420–11430.
[40] Williams, O. F.; Guo, Z. K.; Hu, J.; Yan, L.; You, W.; Moran, A. M. Energy transfer mechanisms in layered 2D perovskites. *J. Chem. Phys.* **2018**, *148*, 134706.
[41] Chen, X. H.; Lu, H. P.; Li, Z.; Zhai, Y. X.; Ndione, P. F.; Berry, J. J.; Zhu, K.; Yang, Y.; Beard, M. C. Impact of layer thickness on the charge carrier and spin coherence lifetime in two-dimensional layered perovskite single crystals. *ACS Energy Lett.* **2018**, *3*, 2273–2279.
[42] Gao, W.; Wei, Q.; Wang, T.; Xu, J. T.; Zhuang, L. C.; Li, M. J.; Yao, K.; Yu, S. F. Two-photon lasing from two-dimensional homologous ruddlesden-popper perovskite with giant nonlinear absorption and natural microcavities. *ACS Nano* **2022**, *16*, 13082–13091.
[43] Dhanabalan, B.; Leng, Y. C.; Biffi, G.; Lin, M. L.; Tan, P. H.; Infante, I.; Manna, L.; Arciniegas, M. P.; Krahne, R. Directional anisotropy of the vibrational modes in 2D-layered perovskites. *ACS Nano* **2020**, *14*, 4689–4697.
[44] Tekelenburg, E. K.; Kahmann, S.; Kamminga, M. E.; Blake, G. R.; Loi, M. A. Elucidating the structure and photophysics of layered perovskites through cation fluorination. *Adv. Opt. Mater.* **2021**, *9*, 2001647.
[45] Ren, E. L.; Zhang, C. Y.; Wang, F. C.; Kong, J. F.; Li, L.; Chen, J.; Xu, J. Y.; Zhang, Y. Synthesis of Cs^+-tuned $(PEA)_2PbI_4$ perovskite

thin films by one-step spin coating. *ECS J. Solid State Sci. Technol.* **2023**, *12*, 026003.

[46] Sun, Q.; Zhao, C. Y.; Yin, Z. X.; Wang, S. P.; Leng, J.; Tian, W. M.; Jin, S. Y. Ultrafast and high-yield polaronic exciton dissociation in two-dimensional perovskites. *J. Am. Chem. Soc.* **2021**, *143*, 19128–19136.

[47] He, H. P.; Yu, Q. Q.; Li, H.; Li, J.; Si, J. J.; Jin, Y. Z.; Wang, N. N.; Wang, J. P.; He, J. W.; Wang, X. K. et al. Exciton localization in solution-processed organolead trihalide perovskites. *Nat. Commun.* **2016**, *7*, 10896.

[48] Zhong, Y. G.; Liao, K.; Du, W. N.; Zhu, J. R.; Shang, Q. Y.; Zhou, F.; Wu, X. X.; Sui, X. Y.; Shi, J. W.; Yue, S. et al. Large-scale thin $CsPbBr_3$ single-crystal film grown on sapphire via chemical vapor deposition: Toward laser array application. *ACS Nano* **2020**, *14*, 15605–15615.

[49] Yantara, N.; Bruno, A.; Iqbal, A.; Jamaludin, N. F.; Soci, C.; Mhaisalkar, S.; Mathews, N. Designing efficient energy funneling kinetics in ruddlesden-popper perovskites for high-performance light-emitting diodes. *Adv. Mater.* **2018**, *30*, 1800818.

[50] Wang, S.; Ma, J. Q.; Li, W. C.; Wang, J.; Wang, H. Z.; Shen, H. Z.; Li, J. Z.; Wang, J. Q.; Luo, H. M.; Li, D. H. Temperature-dependent band gap in two-dimensional perovskites: Thermal expansion interaction and electron–phonon interaction. *J. Phys. Chem. Lett.* **2019**, *10*, 2546–2553.

[51] Yu, S. H.; Xu, J.; Shang, X. Y.; Ma, E.; Lin, F. L.; Zheng, W.; Tu, D. T.; Li, R. F.; Chen, X. Y. Unusual temperature dependence of bandgap in 2D inorganic lead-halide perovskite nanoplatelets. *Adv. Sci.* **2021**, *8*, 2100084.

[52] Zhang, H. C.; Bi, Z. X.; Zhai, Z. H.; Gao, H.; Liu, Y. W.; Jin, M. L.; Ye, M.; Li, X. Z.; Liu, H. W.; Zhang, Y. G. et al. Revealing unusual bandgap shifts with temperature and bandgap renormalization effect in phase-stabilized metal halide perovskite thin films. *Adv. Funct. Mater.* **2024**, *34*, 2302214.

[53] Wei, K.; Xu, Z. J.; Chen, R. Z.; Zheng, X.; Cheng, X. G.; Jiang, T. Temperature-dependent excitonic photoluminescence excited by two-photon absorption in perovskite $CsPbBr_3$ quantum dots. *Opt. Lett.* **2016**, *41*, 3821–3824.

[54] Kahmann, S.; Shao, S. Y.; Loi, M. A. Cooling, scattering, and recombination-the role of the material quality for the physics of tin halide perovskites. *Adv. Funct. Mater.* **2019**, *29*, 1902963.

[55] Neutzner, S.; Thouin, F.; Cortecchia, D.; Petrozza, A.; Silva, C.; Kandada, A. R. S. Exciton–polaron spectral structures in two-dimensional hybrid lead-halide perovskites. *Phys. Rev. Mater.* **2018**, *2*, 064605.

[56] Fang, H. H.; Wang, F.; Adjokatse, S.; Zhao, N.; Even, J.; Loi, M. A. Photoexcitation dynamics in solution-processed formamidinium lead iodide perovskite thin films for solar cell applications. *Light Sci. Appl.* **2016**, *5*, e16056.

[57] Qin, Y.; Li, J. Z.; Hu, J. G.; He, T. C. Optical properties of two-dimensional/three-dimensional composite perovskite films. *J. Phys. Chem. C* **2024**, *128*, 1202–1206.

[58] Wang, Y. N.; Song, F. L.; Yuan, Y.; Dang, J. C.; Xie, X.; Sun, S. B.; Yan, S.; Hou, Y. B.; Lou, Z. D.; Xu, X. L. Strong triplet-exciton–LO-phonon coupling in two-dimensional layered organic-inorganic hybrid perovskite single crystal microflakes. *J. Phys. Chem. Lett.* **2021**, *12*, 2133–2141.

[59] Xu, J. Y.; Guo, Z. L.; Zhou, Q. H.; Wang, Y. X.; Xue, Z.; Han, Y. D.; Yang, W. S.; Ma, X. N. Exciton–phonon coupling and vibronic emission structure in 2D perovskite thin films with naphthylmethylamine spacers. *J. Phys. Chem. C* **2023**, *127*, 18431–18441.

[60] Lee, J. W.; Dai, Z. H.; Han, T. H.; Choi, C.; Chang, S. Y.; Lee, S. J.; De Marco, N.; Zhao, H. X.; Sun, P. Y.; Huang, Y. et al. 2D perovskite stabilized phase-pure formamidinium perovskite solar cells. *Nat. Commun.* **2018**, *9*, 3021.

[61] Wang, R.; Xue, J. J.; Meng, L.; Lee, J. W.; Zhao, Z. P.; Sun, P. Y.; Cai, L.; Huang, T. Y.; Wang, Z. X.; Wang, Z. K. et al. Caffeine improves the performance and thermal stability of perovskite solar cells. *Joule* **2019**, *3*, 1464–1477.

[62] Guo, Z. Y.; Zhang, Y.; Wang, B. Z.; Wang, L. D.; Zhou, N.; Qiu, Z. W.; Li, N. X.; Chen, Y. H.; Zhu, C.; Xie, H. P. et al. Promoting energy transfer via manipulation of crystallization kinetics of quasi-2D perovskites for efficient green light-emitting diodes. *Adv. Mater.* **2021**, *33*, 2102246.

[63] Guo, Z.; Wu, X. X.; Zhu, T.; Zhu, X. Y.; Huang, L. B. Electron–phonon scattering in atomically thin 2D perovskites. *ACS Nano* **2016**, *10*, 9992–9998.

[64] Do, T. T. H.; Del Águila, A. G.; Xing, J.; Liu, S.; Xiong, Q. H. Direct and indirect exciton transitions in two-dimensional lead halide perovskite semiconductors. *J. Chem. Phys.* **2020**, *153*, 064705.

[65] Liu, Z. Y.; Chen, Y. Y.; Li, J. Z.; Yao, W. D.; Luo, T.; Li, D. H. Probing local structural phase transition at the surface of $(BA)_2PbI_4$ via interlayer exciton emission. *Adv. Funct. Mater.* **2024**, *34*, 2312074.

[66] Debasu, M. L.; Ananias, D.; Macedo, A. G.; Rocha, J.; Carlos, L. D. Emission-decay curves, energy-transfer and effective-refractive index in Gd_2O_3: Eu^{3+} nanorods. *J. Phys. Chem. C* **2011**, *115*, 15297–15303.

[67] Baur, F.; Glocker, F.; Jüstel, T. Photoluminescence and energy transfer rates and efficiencies in Eu^{3+} activated $Tb_2Mo_3O_{12}$. *J. Mater. Chem. C* **2015**, *3*, 2054–2064.

[68] Zheng, W. H.; Liu, H. W.; Xu, J.; Jiang, Y.; Fan, P.; Huang, W.; Jiang, F.; Li, L. H.; Fan, X. P.; Zhu, X. L. et al. Carrier-funneling-induced efficient energy transfer in CdS_xSe_{1-x} heterostructure microplates. *ACS Energy Lett.* **2019**, *4*, 2796–2804.